Green Chemistry

ROYAL SOCIETY OF CHEMISTRY

PAPER

View Article Online
View Journal | View Issue

Cite this: *Green Chem.*, 2024, **26**, 6511

Selective hydrogenolysis of furfural to 1,2-pentanediol over a Pt–Fe/MT catalyst under mild conditions†

Chen Cao,‡[a,b] Weixiang Guan,‡[a] Qiaoyun Liu,[c] Lin Li,[a] Yang Su,[a] Fei Liu,*[a] Aiqin Wang *[a] and Tao Zhang*[a]

Received 4th February 2024,
Accepted 17th April 2024

DOI: 10.1039/d4gc00642a

rsc.li/greenchem

Furfural is a large-volume and widely available biomass-derived platform compound, and its transformation into valuable pentanediols is important for the sustainable production of bio-based polymers. Herein, we report a new catalyst system composed of Pt–Fe bimetallic nanoparticles highly dispersed on a commercial magnesium titanate (MT) support. HAADF-STEM, CO-DRIFTS and XPS characterization studies revealed that Pt was in the metallic state with a particle size of 1–2 nm, while Fe existed as Fe^{2+} and was decorated on the Pt particles. The electron transfer from Fe to Pt weakened the hydrogenation activity of the furan ring and meanwhile promoted selective ring-opening to 1,2-pentanediol (1,2-PeD). Reaction kinetics studies revealed the reaction rate with respect to hydrogen pressure was close to zero order, which allowed the reaction to proceed at a hydrogen pressure as low as 0.1 MPa. Under mild conditions of 140 °C and 0.1 MPa, the 0.1Pt0.05Fe/MT catalyst offered by far the highest production rate of 178 mol 1,2-PeD per mol Pt per hour, and the Pt–Fe bimetallic catalyst was stable during 200 h of time-on-stream, showing great potential for practical applications.

Introduction

Furfural (FA), as an important platform molecule derived from biomass, is being considered as a promising feedstock for producing valuable pentanediols including 1,2-pentanediol (1,2-PeD),[1,2] 1,4-pentanediol (1,4-PeD)[3,4] and 1,5-pentanediol (1,5-PeD).[5] Among these, 1,2-PeD has attracted increasing attention due to its widespread applications in the fields of polyesters, fungicides, disinfectants and cosmetics. Compared with conventional approaches to producing 1,2-PeD, which involve the use of fossil resources and multi-steps of oxidation and hydrolysis, the selective hydrogenolysis of FA to 1,2-PeD is a sustainable, environmentally friendly, and one-step approach. As shown in Scheme 1, the key to this approach is the precise cleavage of the C_5–O bond of the furan ring while avoiding the breakage of the C_2–O bond as well as the hydrogenation of the furan ring, which requires the delicate design of catalysts for balancing the activities for hydrogenolysis and hydrogenation. Oxide-supported noble metal catalysts have been extensively investigated for this reaction, and the nature of the support has been found to play an important role far beyond dispersing the active metal. It has been accepted that a basic support, in cooperation with the highly dispersed metal species thereon, is conducive to the selective formation of 1,2-PeD. For example, Ru/MnO_x,[6] Pt/HT (HT refers to hydrotalcite),[1] Rh/OMS-2,[7] Ru/MgO,[8] Pt/CeO_2[2,9] and Pt/Mg(Al)

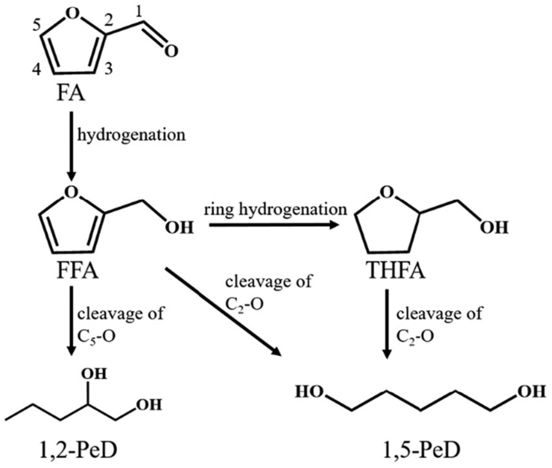

Scheme 1 The reaction routes for hydrogenolysis of furfural.

---

[a] CAS Key Laboratory of Science and Technology on Applied Catalysis, Dalian Institute of Chemical Physics, Chinese Academy of Sciences, Dalian 116023, China. E-mail: fei.liu@dicp.ac.cn, aqwang@dicp.ac.cn, taozhang@dicp.ac.cn
[b] University of Chinese Academy of Sciences, Beijing 100049, China
[c] College of Chemistry, Zhengzhou University, Zhengzhou, 450001, China

† Electronic supplementary information (ESI) available. See DOI: https://doi.org/10.1039/d4gc00642a

‡ These authors contributed equally.

O@Al_2O_3[10] were all reported to be active and selective for the production of 1,2-PeD from FA or furfuryl alcohol (FFA). In particular, a 1%Rh/OMS-2 catalyst has afforded a 1,2-PeD yield as high as 87% under the reaction conditions of 160 °C and 3 MPa H_2,[7] which was the best result reported so far. In spite of these significant advances, the atom utilization of precious metals is not satisfactorily high, which will limit practical applications due to the high cost of precious metals. Moreover, a high yield of 1,2-PeD is usually achieved under relatively high hydrogen pressures (typically 1–5 MPa), which requires additional energy input. Therefore, it is highly desirable to design a more efficient catalyst that has a sufficiently high noble metal atom utilization efficiency and is able to run the reaction under milder conditions.

The most effective approach to enhancing the precious metal atom efficiency is to synthesize single-atom catalysts (SACs).[11–13] Nevertheless, it has been demonstrated that when Pt was dispersed as single atom species at a pretty low loading (0.08 wt%) on a HT-derived oxide support, the selectivity to ring-opening of FFA decreased significantly compared to the nanoparticle counterpart.[10] Obviously, SACs are less effective in cleaving the C–O bonds of the furan ring due to limited hydrogenolysis activity. On the other hand, by introducing a second metal promoter to modify the electronic and geometric properties of the active precious metal, both activity and selectivity could be enhanced for C–O bond hydrogenolysis reactions,[14–21] which provides an alternative route to increase the precious metal utilization efficiency. For the hydrogenolysis of tetrahydrofurfuryl alcohol (THFA) developed by Tomishige and coworkers, when introducing a second metal Re or Mo to Rh/SiO_2 or Ir/SiO_2, both the activity and selectivity to 1,5-PeD were greatly enhanced.[15–17,22,23] Recently, Upare *et al.* reported that Ru_3Sn_7/ZnO offered a high yield (84.7%) of 1,2-PeD for the hydrogenolysis of FA, in sharp contrast to monometallic Ru/ZnO over which FFA was the primary product.[24] These examples provide evidence of the effectiveness of a bimetallic strategy in promoting the C–O hydrogenolysis of biomass-derived molecules although the precious metal efficiency has yet to be further enhanced.

In this work, we report a new catalyst system, Pt–Fe/MT (MT refers to magnesium titanate), which is able to catalyze the FA/FFA hydrogenolysis reaction under a hydrogen pressure as low as 0.1 MPa and offers a production rate of up to 178 mol 1,2-PeD per mol Pt per hour, which is the best result reported so far. The biomass-derived feedstock, the green solvent (water), the mild reaction conditions, as well as the recyclable solid catalyst make the process sustainable and environmentally friendly.

Experiment

Catalyst preparation

The Pt–Fe/MT catalysts were prepared by an incipient wetness co-impregnation method. In detail, the as-received MT support (Aladdin) was calcined at 800 °C for 5 h before use. 0.137 g of an aqueous solution of chloroplatinic acid hexahydrate ($H_2PtCl_6·6H_2O$, Aladdin, Pt: 5.84 wt%) and 0.192 g of an aqueous solution of iron nitrate nonahydrate ($Fe(NO_3)_3·9H_2O$, Aladdin, Fe: 2.08 wt%) were dissolved in 0.5 g of water, to which 1 g of MT was added and then allowed to stand for 24 h. The resulting catalyst precursor was dried at 80 °C for 12 h and calcined at 300 °C for 3 h, followed by reduction in H_2 at 300 °C for 30 min. After cooling to room temperature in H_2, the sample was passivated with 1%O_2/N_2 for at least 4 h to obtain 0.8 wt% Pt–0.4 wt% Fe/MT catalyst, which was denoted as 0.8Pt0.4Fe/MT. A series of catalysts with different Pt and Fe contents were prepared for comparison and denoted as *x*Pt*y*Fe/MT, where x and y represent the weight percentage of Pt and Fe, respectively.

Characterization

The powder X-ray diffraction (XRD) patterns were recorded in the range from 10 to 80° on an X'pert Pro-1 diffractometer equipped with a Cu Kα radiation source (λ = 0.15432 nm) operated at 40 kV and 40 mA.

High angle annular dark field scanning transmission electron microscopy (HAADF-STEM) images were obtained on a JEOL JEM-2100F instrument. Before imaging, the passivated sample was ultrasonically dispersed in ethanol, and then dropped on lacey-carbon-coated copper TEM grids.

The chemisorption of CO and H_2 was performed on a Micromeritics AutoChem II 2920 chemisorber. Prior to the measurement, the calcined sample of 100 mg was pretreated at 300 °C in pure H_2 for 30 min, and then purged in an inert gas flow (He for CO chemisorption and Ar for H_2 chemisorption) at 310 °C for 30 min. When the sample was cooled down to 50 °C, pulses of 5%CO/He or 10%H_2/Ar were introduced for CO or H_2 chemisorption until saturation. The consumed CO or H_2 was detected with a TCD and quantified by calibration with predetermined volumes of standard gas.

CO_2-temperature-programmed desorption (TPD) and NH_3-TPD were performed on the same chemisorber as used for the chemisorption of CO and H_2. The pretreatment conditions were the same as those for CO chemisorption. After the pretreatment, the sample was cooled to 50 °C for CO_2-TPD and 100 °C for NH_3-TPD and subsequently exposed to pulses of CO_2 or 10% NH_3/He until saturation was reached. Then, the sample underwent He purging until a smooth baseline was obtained, followed by heating to 800 °C in He with a flow rate of 30 mL min^{-1} and a ramp rate of 10 °C min^{-1}. The desorbed CO_2 or NH_3 was detected and quantified using mass spectrometry (MS) signals with m/z = 44 for CO_2 and 16 for NH_3.

The quasi *in situ* X-ray photoelectron spectroscopy (XPS) was performed on a Thermofisher Escalab 250 Xi+ spectrometer equipped with an Al Kα X-ray source. Prior to the measurement, the calcined sample was pre-reduced at 300 °C for 30 min, and then transferred to the measurement chamber without exposure to air. The binding energies of both Pt and Fe were calibrated using the C 1s peak at 284.8 eV from adventitious carbon.

Diffuse reflectance infrared Fourier transform spectra (DRIFTS) of CO adsorbed on different catalysts were recorded on a Bruker Equinox 55 spectrometer equipped with an MCT detector with a resolution of 4 cm^{-1}. The calcined sample was loaded into the infrared cell and reduced at 300 °C for 30 min under H_2 followed by purging with He at 310 °C for 20 min. After cooling down to room temperature, the background spectrum was recorded. Subsequently, 6%CO/He was introduced for adsorption and the spectra were recorded until the band intensity no longer changed. Then, the flow gas was switched to He to purge the gas phase CO and the CO was physically adsorbed until the band intensity no longer changed. The spectra were recorded at the steady state.

Reaction tests

The catalysts were evaluated in a 50 mL Teflon-lined stainless steel autoclave. For each test, 100 mg of FA, 100 mg of a passivated catalyst and 5 mL of H_2O were added into the autoclave. The autoclave was sealed, flushed with H_2 at least 5 times, and then charged with H_2 until the desired pressure. The reaction was conducted at 140 °C for 10 h with a stirring rate of 800 rpm. After the reaction, the liquid phase was separated from the catalyst by centrifugation and analyzed using a gas chromatograph (Agilent 7890B) equipped with an FID detector and FFAP column using 1,4-dioxane as the internal standard.

For investigating the change of conversion/selectivity with the reaction time, the test was performed in a 100 mL stainless steel autoclave equipped with a mechanical agitator and sampling valve. Thus, 1 g of catalyst, 1 g of FA and 50 mL of H_2O were charged into the reactor and the reaction was conducted at 140 °C and 1 MPa H_2. Liquid samples were taken at 0, 30, 120, 300, 480, and 600 min during the reaction, with approximately 0.7 mL collected each time.

The stability of the 0.8Pt0.4Fe/MT catalyst was evaluated in a continuous flow fixed-bed reaction system at 140 °C and 1 MPa H_2. 3 g of catalyst was loaded into the middle part of the stainless steel tubular reactor (internal diameter 9 mm, length 370 mm), with the upstream and downstream sections packed with quartz sand and separated from the catalyst bed with quartz wool. The catalyst was reduced *in situ* by H_2 at 300 °C for 30 min prior to the reaction, with a flow rate of 30 mL min^{-1}. After cooling down to 140 °C under the H_2 flow, an aqueous solution of 2 wt% FA was fed into the reactor through a high-pressure liquid pump with a flow rate of 0.007 mL min^{-1}, affording a liquid-hour space velocity (LHSV) of 0.15 h^{-1}, while H_2 was co-fed to the reactor at a flow rate of 8 mL min^{-1}, corresponding to a gas-hour space velocity (GHSV) of 171 h^{-1}. The effluent gas and liquid were separated by a condenser, and the liquid product was analyzed as described above.

Results and discussion

Structural characterization

The series of PtFe/MT catalysts was characterized to obtain structural information. The XRD patterns show the characteristic peaks of the MT support composed of $MgTiO_3$ and Mg_2TiO_4 mixed phases (Fig. S1†). The absence of XRD peaks due to Pt or Fe/FeO_x crystalline phases suggests the high dispersion of the two components. Fig. 1 shows the HAADF-STEM and HRTEM images of the 0.8Pt/MT and 0.8Pt0.4Fe/MT catalysts. It can be seen that for both catalysts, the particles are uniformly dispersed on the MT support surface with an average size of only 1–2 nm (Fig. 1a and b). This is surprising when considering the MT support has a pretty low surface area (5 m^2 g^{-1}). Compared with 0.8Pt/MT catalyst, the introduction of Fe did not result in the growing of particles; instead, the average particle size in the 0.8Pt–0.4Fe/MT catalyst was even smaller. The HRTEM image (Fig. 1c) of the 0.8Pt0.4Fe/MT catalyst clearly shows the lattice fringes with a spacing of 0.222 nm of the Pt (111) surface. Careful inspections of many randomly selected areas did not show any signs of the Pt–Fe alloy phase, which is most likely due to the moderate reduction temperature (300 °C) employed in this work. The irregular shape and morphology of nanoparticles suggest a strong interaction of Pt with the support. The complete overlapping of Pt and Fe signals in both the line-scan (Fig. 1d and e) of individual particles and the elemental mapping (Fig. 1f) of the randomly selected area indicates that Fe is directly interacting with Pt, rather than being separately dispersed on the MT surface.

The basic physico-chemical properties of the catalysts are listed in Table 1. The loading of Pt and Fe onto the MT support resulted in a significant increase in the surface area from 5 to 23 m^2 g^{-1}, which was probably due to the etching effect of acid precursors on the two metals with the basic support to create a porous structure. In fact, Mg^{2+} was detected in the impregnation solution (Table S1†), indicating the generation of defect sites during the impregnation process, which will facilitate the anchoring of Pt onto the support. CO_2-TPD and NH_3-TPD were conducted to evaluate the acidity and basicity of the catalysts. For the CO_2-TPD, the 0.8Pt0.4Fe/MT catalyst gave an uptake of 37 μmol_{CO_2} g_{cat}^{-1}, significantly lower than that on the 0.8Pt/MT catalyst (85.2 μmol_{CO_2} g_{cat}^{-1}); meanwhile, the CO_2 desorbed at a lower temperature (Fig. S2†), suggesting that the introduction of Fe species leads to a decrease in both the uptake amount and strength of basicity. For the NH_3-TPD, it was found that the presence of Fe caused a slight increase in the NH_3 uptake, while a new and intense desorption peak was produced at around 200 °C along with the peak weakening at around 400 °C (Fig. S3†). This result indicated that the addition of Fe species weakened the strong acidity and increased the number of weak acid sites. For CO chemisorption, the CO uptake decreased monotonically with an increase of Fe content, which could be ascribed to the electronic modification of Pt by Fe[25] as well as the partial coverage of the Pt surface by excess Fe.[17] In contrast, the H_2 uptake decreased first at low Fe content and then increased and reached its maximum on the 0.8Pt0.4Fe/MT catalyst, and then decreased again at higher Fe content. This trend could be justified by hydrogen spillover, which is well known to occur between Pt and reducible oxide, such as FeO_x.[26,27] Herein we use the H/CO ratio to signify the extent of hydrogen spillover. It shows a monotonically increasing trend with the Fe content,

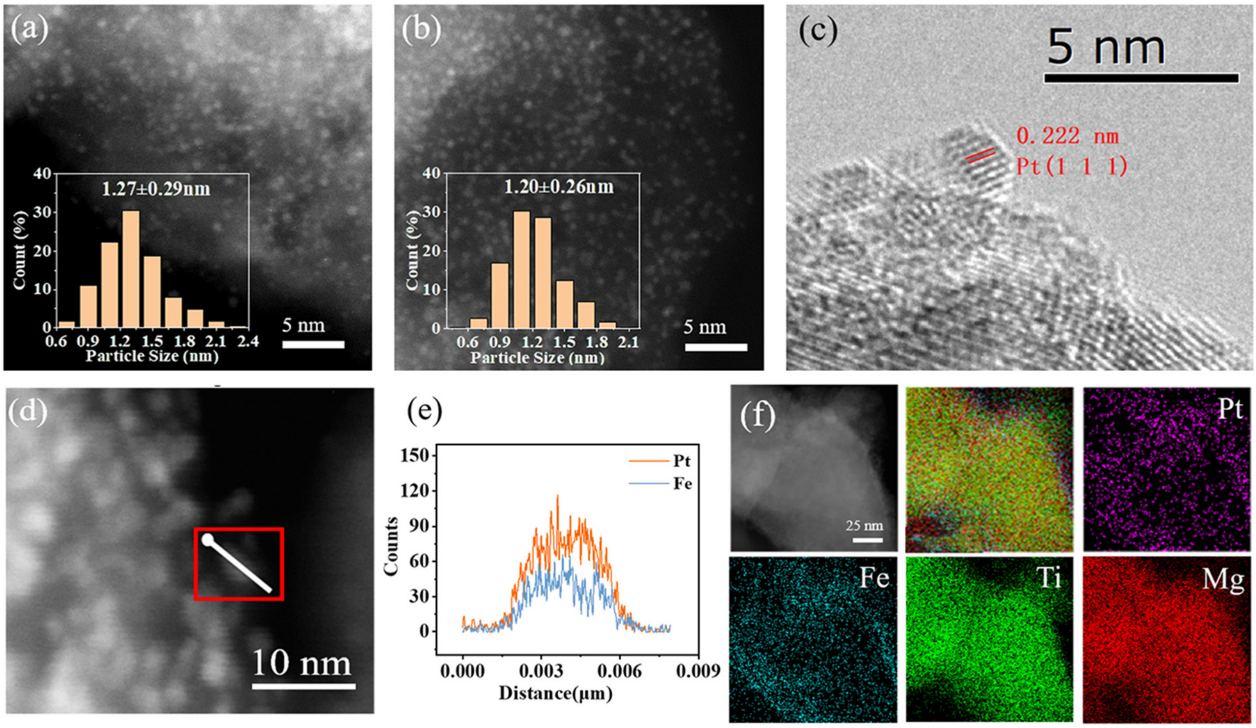

Fig. 1 HAADF-STEM images of (a) the 0.8Pt/MT and (b) the 0.8Pt0.4Fe/MT catalysts; (c) HRTEM image of the 0.8Pt0.4Fe/MT catalyst; (d–f) line-scan and elemental mapping images of the 0.8Pt0.4Fe/MT catalyst.

Table 1 Basic physico-chemical properties of different catalysts

				CO		H_2		
Catalysts	S_{BET} (m^2 g^{-1})	CO_2 uptake[a] (μmol_{CO_2} g_{cat}^{-1})	NH_3 uptake[b] (μmol_{NH_3} g_{cat}^{-1})	Uptake[c] (μmol g^{-1})	Dispersion (%)	Uptake[c] (μmol g^{-1})	Dispersion (%)	H/CO
MT	5	76.1	8.9	—	—	—	—	—
0.8Pt/MT	12	85.2	11.8	11.4	27.8	6.0	29.3	1.05
0.8Pt0.1Fe/MT	—	—	—	8.0	19.4	5.2	25.5	1.30
0.8Pt0.4Fe/MT	23	37.0	15.6	5.2	12.6	8.5	41.6	3.27
0.8Pt0.8Fe/MT	—	—	—	2.3	5.7	6.5	31.9	5.65

[a] Determined by CO_2-TPD using an MS signal $m/z = 44$. [b] Determined by NH_3-TPD using an MS signal $m/z = 16$. [c] Dispersion is determined by assuming CO/Pt = 1, H_2/Pt = 0.5.

demonstrating that the presence of Fe/FeO_x promoted hydrogen spillover. It is noted that for the 0.8Pt0.8Fe/MT catalyst, in spite of a high H/CO ratio, the uptake of both H_2 and CO is much lower than that on the 0.8Pt0.4Fe/MT catalyst due to partial coverage of the Pt surface by excess Fe. Moreover, it should be pointed out that the dispersions of the catalysts determined either by CO chemisorption or by H_2 chemisorption were considerably lower than that determined by average particle size with HAADF-STEM imaging, which could be explained by the significant weakening of the CO/H_2 chemisorption due to strong electronic interaction between Pt and FeO_x. Similar phenomena were also previously observed in other systems.[20,28,29]

The electronic properties of Pt and Fe in these PtFe/MT catalysts were characterized by CO-DRIFTS and XPS. As shown in Fig. 2, the adsorption of CO on the 0.8Pt/MT catalyst produced a broad major band in the 2000–2100 cm^{-1} region assigned to linearly adsorbed CO and a minor broad band in the 1700–1900 cm^{-1} region assigned to bridge-adsorbed CO.[30,31] The former band could be further deconvoluted into three bands at 2084 cm^{-1}, 2061 cm^{-1} and 2023 cm^{-1}, which could be ascribed to Pt sites with different coordinations; the lower frequency means a lower coordination number of Pt.[32] Compared with 0.8Pt/MT, the 0.8Pt0.4Fe/MT catalyst presented similar CO-DRIFTS features but the bands shifted to lower frequencies with decreased intensities. The red-shift of the bands suggested increased electron density on the Pt sites by the donation from Fe sites,[25,33] and the lower intensity was in agreement with CO chemisorption data indicating the number of available Pt sites was reduced due to the partial coverage by

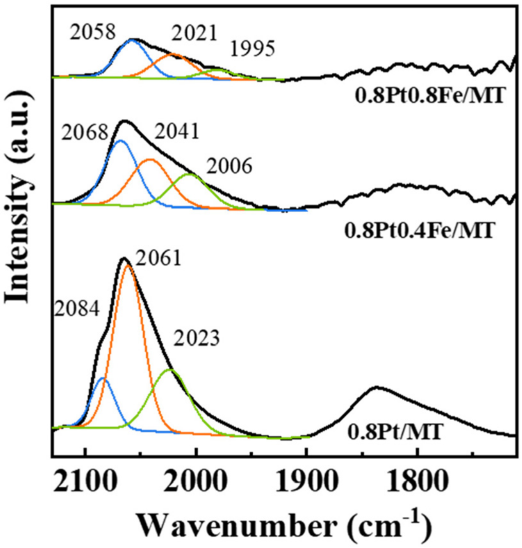

Fig. 2 CO-DRIFTS of different Pt–Fe/MT catalysts.

Fe/FeO$_x$. With an increase of the Fe content, this trend became more pronounced.

The electronic interaction between Pt and Fe could be further corroborated by pseudo *in situ* XPS. As shown in Fig. 3, the binding energy of Pt 4f$_{7/2}$ was centered at 71.4 eV for the freshly reduced 0.8Pt/MT catalyst, indicating that Pt was mainly in its metallic state (Pt^0).[34] Compared to it, the 0.8Pt0.4Fe/MT catalyst showed the Pt 4f$_{7/2}$ peak at a binding energy of 71.2 eV, suggesting electron transfer from Fe to Pt, which was in line with the CO-DRIFTS result. On the other hand, Fe 2p XPS showed the binding energy of Fe 2p$_{3/2}$ was at 709.7 eV for the 0.8Pt0.4Fe/MT catalyst, indicating the dominance of Fe^{2+}.[35] This was in contrast to the Pt-free 0.4Fe/MT sample, which showed Fe 2p$_{3/2}$ at a binding energy of 711.7 eV, characteristic of Fe^{3+}.[36] Obviously, the hydrogen spillover from Pt to Fe promoted the reduction of Fe^{3+} to Fe^{2+} at the relatively low temperature of 300 °C. It was earlier reported that the presence of low-valence transition metal cations was beneficial to the adsorption of oxygen-containing groups due to their oxyphilic nature.[13,20,21] Therefore, it can be expected that the Fe^{2+} species, in conjunction with the metallic Pt, will be favourable to the selective cleavage of the C–O bond of FA/FFA.

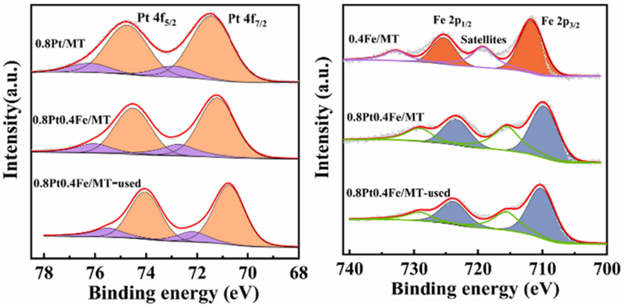

Fig. 3 XPS Pt 4f and Fe 2p spectra of different Pt–Fe/MT catalysts.

Catalytic performances

The catalytic performances of the series of PtFe/MT catalysts are summarized in Table 2. Over all the catalysts investigated, FA was converted completely due to its high reactivity, but product selectivities varied and were highly dependent on the Pt/Fe ratio. For the monometallic 0.8Pt/MT catalyst, the selectivities to 1,2-PeD and 1,5-PeD were 54% and 17%, respectively, indicating that the hydrogenative ring-opening reactions dominated under the reaction conditions. Meanwhile, a selectivity of 22% to THFA indicated that furan ring hydrogenation took place to a certain extent, along with the ring-opening reactions. In order to increase ring-opening selectivity, the ring-hydrogenation reaction must be suppressed because THFA, upon being formed, the ring could no longer be opened (Table S3†). Interestingly, when a second component, Fe, was present in the catalysts, even in a very small amount (entries 2 and 3, Table 2), the formation of THFA was greatly suppressed and the selectivity to ring-opening products increased remarkably. In particular, the 0.8Pt0.4Fe/MT catalyst gave rise to 76% selectivity to 1,2-PeD and 18% to 1,5-PeD, a total of 94% selectivity to ring-opening products, while the hydrogenation side-products that included FFA, THFA and 1-pentanol (1-PO) were marginal. Moreover, when the concentration of FFA was raised to 10 wt% while the substrate/catalyst was kept unchanged, our 0.8Pt0.4Fe/MT catalyst maintained excellent performance, affording complete conversion of FFA and 75% selectivity to 1,2-PeD (entry 5, Table 2). Considering that most

Table 2 Catalytic performances of the Pt-based bimetallic catalysts for furfural hydrogenolysis[a]

		Selectivity (%)					
Entry	Catalyst	1,2-PeD	1,5-PeD	FFA	THFA	1-PO	Ring-opening
1	0.8Pt/MT	54	17	3	22	4	71
2	0.8Pt0.1Fe/MT	63	25	0	9	3	88
3	0.8Pt0.4Fe/MT	76	18	1	2	3	94
4	0.8Pt0.8Fe/MT	48	12	37	1	2	60
5	0.8Pt0.4Fe/MT[b]	75	20	1	2	2	95
6	0.8Pt0.4Co/MT	39	32	4	24	1	71
7	0.8Pt0.4Ni/MT	17	19	0	63	1	36
8	0.8Pt0.4Cu/MT	0	0	94	5	0	0
9	0.4Pt0.2Fe/MT	74	20	2	2	2	94
10	0.2Pt0.1Fe/MT	67	20	9	2	2	87
11	0.1Pt0.05Fe/MT	43	17	36	2	2	60
12	0.1Pt0.03Fe/MT[c]	45	22	20	10	3	67
13	0.8Pt0.4Fe/MT[d]	81	15	0	2	2	96
14	0.2Pt0.1Fe/MT[d]	72	19	5	2	2	91

[a] Reaction conditions: 0.1 g of FA in 5 mL of H_2O, 100 mg of catalyst, 1 MPa H_2, and 140 °C for 10 h. In all these tests, FA was completely converted. [b] 0.5 g of FFA in 4.5 mL of H_2O, 500 mg of catalyst, and 140 °C for 15 h, using the online gas path to maintain a H_2 pressure of 1 MPa during the reaction process. [c] The catalyst was reduced at 500 °C. [d] 0.1 MPa H_2 was used.

of the previous works used very dilute substrate concentrations,[1,37] our present result demonstrated greater potential for practical applications. A further increase of the Fe content, however, led to a significant elevation of the FFA selectivity (entry 4), which should be caused by the partial coverage of active Pt sites by excess Fe resulting in decreases in hydrogenolysis activity. This was consistent with the low chemisorption uptake of CO/H_2 on the 0.8Pt0.8Fe/MT catalyst. The promoting function of Fe to the formation of 1,2-PeD motivated us to investigate other transition metal additives (entries 6–8). In contrast to Fe, the addition of Co to Pt/MT resulted in an increase in the 1,5-PeD selectivity at the expense of 1,2-PeD selectivity, while the addition of Ni led to the predominant formation of THFA and Cu led to up to 94% of FFA selectivity. Obviously, Fe was unique in promoting the ring-opening reaction of FA to 1,2-PeD.

In the above Pt–Fe/MT catalysts, the best-performing catalyst (0.8Pt0.4Fe/MT) had an Fe/Pt atomic ratio of 1.7. Then, we investigated the effect of Pt content by fixing the Fe/Pt ratio of 1.7 with the aim to maximize the Pt atom efficiency. To our delight, when the Pt content was decreased from 0.8% to 0.4%, the 1,2-PeD selectivity as well as the ring-opening selectivity remained almost unchanged (entry 9). Further decreasing the Pt content to 0.2% led to only a slight decrease of the 1,2-PeD selectivity from 74% to 67% along with an increase of FFA selectivity from 2% to 9% (entry 10). When the Pt content was decreased to the extremely low value of 0.1%, the catalyst still maintained high selectivity to ring-opening, reaching 67%, although the 1,2-PeD selectivity declined to 45% (entries 11 and 12). Previously, Zhu *et al.* reported that a 0.13%Pt/Mg(Al)O@Al_2O_3 catalyst could afford 41% selectivity to 1,2-PeD and 9% selectivity to 1,5-PeD, a total of 50% ring-opening selectivity.[10] Compared to that result, our Pt–Fe/MT obviously offered a much higher ring-opening selectivity and a better efficiency of expensive Pt metal, demonstrating the remarkable promoting effect of Fe. As indicated by the CO-DRIFTS and XPS analyses, the electron transfer from Fe^{2+} to Pt made Pt more electron-rich, which suppressed ring hydrogenation at Pt sites. Meanwhile, the low-valence Fe^{2+} sites were reported to selectively adsorb and activate oxygen-containing groups,[13,38] facilitating C–O bond breakage. Therefore, the synergy between Fe^{2+} species and the neighboring Pt^0 sites in the Pt–Fe/MT catalysts with an Fe/Pt ratio of 1–2 should be responsible for the greatly enhanced ring-opening selectivity.

More interestingly, when the reaction was performed at a hydrogen pressure of as low as 0.1 MPa, both the 0.8Pt0.4Fe/MT and the 0.2Pt0.1Fe/MT catalysts were even more selective to ring opening with the complete conversion of FA and up to 81% selectivity to 1,2-PeD (entries 13 and 14, Table 2). To our knowledge, this is the first report where the reaction could be operated at ambient hydrogen pressure. When compared to earlier reported noble metal catalysts, which run the reaction at hydrogen pressures of 1–5 MPa (Table S4†), it is found that our 0.1Pt0.05Fe/MT catalyst gave rise to a production rate of 178 $mol_{1,2\text{-PeD}}\ mol_{Pt}^{-1}\ h^{-1}$ under the reaction conditions of 140 °C and 0.1 MPa H_2, which is the highest production rate reported so far under such mild reaction conditions (Table S4†).

Reaction kinetics and mechanism

To understand the reaction mechanism, the conversion/yields *versus* reaction time relationship was first investigated over the 0.8Pt0.4Fe/MT catalyst with FA and FFA as the substrate (Fig. 4), respectively. When FA was used as the substrate, it was completely converted to FFA even before the reaction temperature reached 140 °C, indicating that FFA was the intermediate for FA hydrogenolysis. Therefore, the kinetic curves, either with FA or FFA as the substrate, look very similar except that the product formation rate was slightly slower when FA was the substrate. Both 1,2-PeD and 1,5-PeD yields increased with reaction time until 10 h. No other byproducts or intermediates were detected during the whole reaction time except for 1,2-PeD, 1,5-PeD, FFA, THFA, and a negligible amount of 1-PO. It was found that the initial formation rate of 1,2-PeD was 3.8 times higher than that of 1,5-PeD, demonstrating the preferential breakage of the C_5–O bond over the Pt–Fe/MT catalyst.

To compare the ring-opening reaction kinetics over 0.8Pt/MT and 0.8Pt0.4Fe/MT catalysts, we used FFA as the substrate and measured the conversion rate of FFA as well as the formation rate of 1,2-PeD and 1,5-PeD by varying the H_2 pressure, FFA concentration and the reaction temperature. The results are shown in Fig. 5, 6 and Fig. S4–S6.† For FFA conversion, it was found that the reaction order with respect to H_2 was almost the same over both catalysts, being close to zero order, in the investigated pressure range of 0.3–3 MPa, which suggests that the Pt surface is saturated with hydrogen and the addition of Fe with an Fe/Pt ratio of 1.7 does not affect the capability of Pt for H_2 activation. The close-to-zero reaction order of H_2 can well explain the excellent performance of the catalysts at ambient hydrogen pressures (entries 13 and 14,

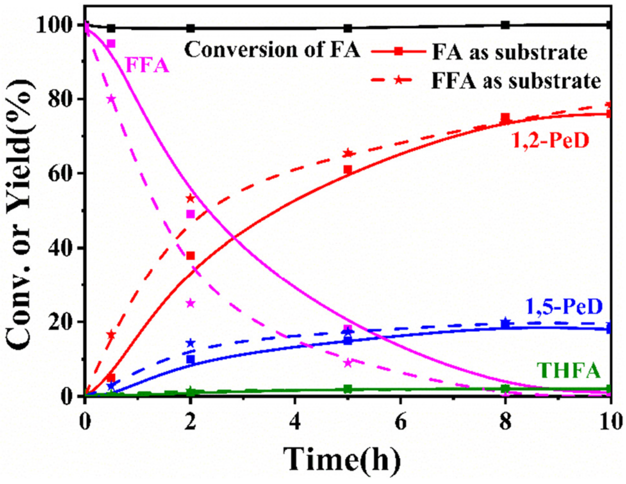

Fig. 4 The conversion of FA and product yields with reaction time for FA and FFA hydrogenolysis reactions. Reaction conditions: 1 g of substrate in 50 g of water, 1 g of 0.8Pt0.4Fe/MT catalyst, 140 °C, and 1 MPa H_2.

Table 2). Considering that water can greatly accelerate hydrogen spillover,[39] the zero-order dependence on hydrogen pressure is assumed to be related to the use of water as the solvent. Indeed, the screening of solvents indicated that water was the most effective solvent for this reaction (Table S5†). Therefore, in this work, water is not only used as the green solvent but, more importantly, it can facilitate the hydrogenolysis reaction *via* mediating hydrogen spillover.

On the other hand, the reaction order with respect to FFA was 0.7, suggesting that there is competitive adsorption between FFA and H_2 and the adsorption of FFA is involved in the rate-determining step. The apparent activation energy over the 0.8Pt/MT catalyst was determined to be 46 kJ mol^{-1} while it was 93 kJ mol^{-1} over the 0.8Pt0.4Fe/MT catalyst. The quite different activation energy over the two catalysts implies that the nature of the active site and the reaction mechanism should change after the addition of Fe to the Pt/MT. Moreover, the higher activation energy over the 0.8Pt0.4Fe/MT catalyst suggests a high temperature would facilitate the ring-opening reaction. Indeed, when the reaction temperature increased from 140 °C to 180 °C, the selectivity to ring opening increased slightly and no C–C bond cleavage byproducts were detected (Fig. S7†).

Based on the above kinetics studies, we can propose a reaction mechanism. First, H_2 is dissociated into two H atoms on the Pt surface, and then the dissociated H atoms spillover the adjacent Fe^{3+} species and promote the reduction of Fe^{3+} to Fe^{2+} and generate oxygen vacancies. The hydrogenation of FA to FFA is very fast and can be completed during the temperature ramping stage, as shown in Fig. 4. The O atom in the furan ring can easily adsorb onto the oxygen vacancy at the interface between Pt and Fe^{2+}, which was evidenced by the furan ring opening using furan as the substrate (Table S6†). Probably, the $O_{hydroxyl}$–C_1–C_2–O_{ring} forms a cyclic structure with the Pt–O_V–Fe sites, which is relatively stable, as proposed by Tomishige *et al.*[40] When the dissociated H attacks the O on the furan ring, the C_5–O bond is more prone to breakage and generates 1-hydroxy-2-pentanone, an intermediate that was detected using MS by Mizugaki and co-workers,[1] whereupon the C═O group then undergoes rapid hydrogenation to produce 1,2-PeD.

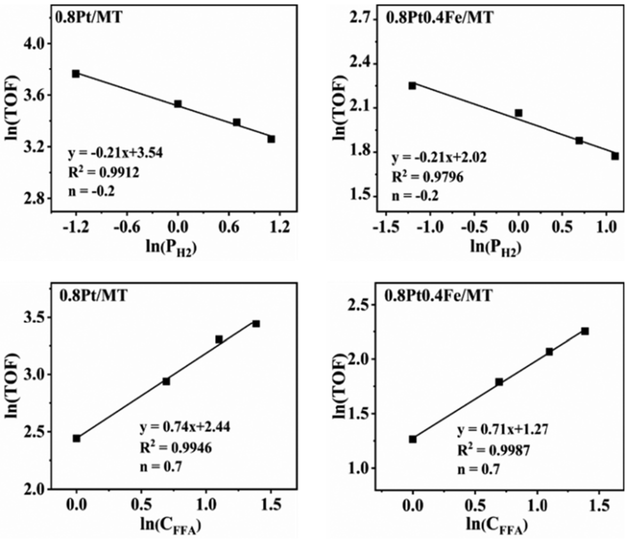

Fig. 5 The reaction rate with respect to hydrogen pressure and FFA concentration over 0.8Pt/MT and 0.8Pt0.4Fe/MT catalysts. Reaction conditions: 10 mg of 0.8Pt/MT or 30 mg of 0.8Pt0.4Fe/MT catalyst, 140 °C. For the hydrogen pressure effect: 0.15 g of FFA in 5 g of water, P_{H_2}: 0.3, 1, 2, 3 MPa; for the FFA concentration effect: 5 g of water, 1 MPa H_2, C_{FFA}: 1%, 2%, 3%, 4%.

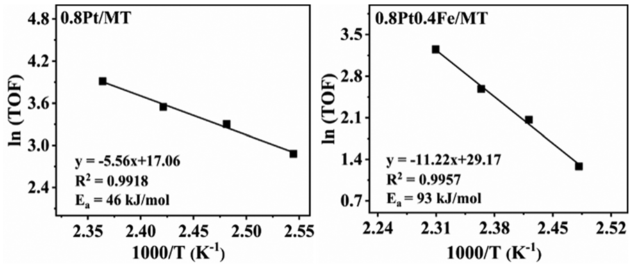

Fig. 6 Arrhenius plots for the FFA hydrogenolysis reaction over the 0.8Pt/MT and 0.8Pt0.4Fe/MT catalysts. Reaction conditions: 0.15 g of FFA in 5 g of water, 1 MPa H_2, 10 mg of 0.8Pt/MT, temperature range of 120–150 °C or 30 mg of 0.8Pt0.4Fe/MT, temperature range of 130–160 °C.

Stability

In addition to activity and selectivity, catalyst stability is also a performance index and even more important with respect to practical applications. In most of the previous studies, the FA to pentanediol reaction has been conducted in batch reactors,[6,7,24,37] which limits the evaluation of the long-term stability of catalysts. In this work, on the basis of catalyst screening, we further evaluated the 0.8Pt0.4Fe/MT catalyst for long-term operation in a continuous fixed-bed reactor, and the result is shown in Fig. 7. The catalyst behaved rather stably during 200 h of time-on-stream. The XPS analysis of the used catalyst showed that Pt^0 became slightly more electron-rich and Fe^{2+} remained unchanged after the reaction (Fig. 3). HAADF-STEM images of the used catalyst (Fig. S8†) revealed that Pt–Fe nanoparticles remained highly dispersed without obvious sintering, indicating that the nanostructure of the active sites was not destroyed during long-term reactions. This excellent stability could be attributed to the strong interaction between Pt and the MT support. The generation of cation defect sites during impregnation facilitated the anchoring of Pt cations to the support, which was evidenced by the presence of a small proportion of Pt^{2+} as detected by XPS (Fig. 3). This proportion of Pt^{2+} acted as an interface nanoglue[41,42] to strengthen the interaction between Pt nanoparticles and the MT support, furnishing the catalyst with superior stability during the reaction.

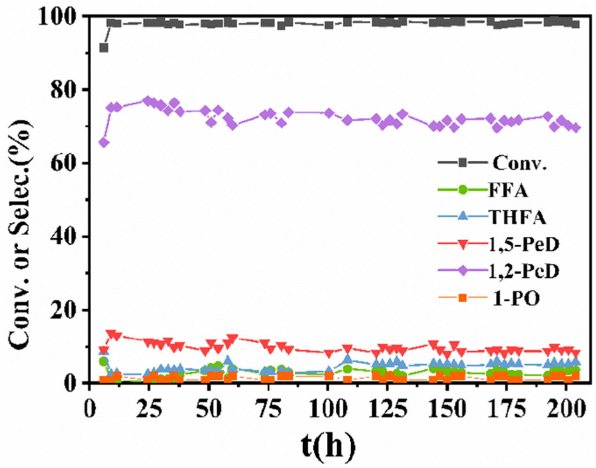

Fig. 7 Long-term stability test of the 0.8Pt0.4Fe/MT catalyst. Reaction conditions: 140 °C, 1 MPa H_2; liquid flow rate: 0.007 mL min^{-1}; gas flow rate: 8 mL min^{-1}; 2 wt% FA aqueous solution, 3 g of catalyst.

Conclusions

We have developed highly active and selective bimetallic PtFe/MT catalysts with an Fe/Pt atomic ratio of 1–2 in which both Pt and Fe were highly dispersed and in intimate contact with each other. The electron transfer from Fe to Pt weakened the ring-hydrogenation activity at Pt sites while the presence of low-valence Fe (mainly Fe^{2+}) promoted the ring-opening reaction, leading to high selectivity to 1,2-PeD. Moreover, the kinetics studies revealed the reaction rate was close to zero with respect to hydrogen pressure, which enabled the hydrogenolysis of FA/FFA to 1,2-PeD to proceed under a hydrogen pressure as low as 0.1 MPa. Under optimized reaction conditions, the catalyst gave rise to a production rate of up to 178 mol 1,2-PeD per mol Pt per hour, which is the best result reported so far. The catalyst was rather stable during the 200 h of time-on-stream, demonstrating the great potential for practical applications. The bimetallic strategy comprising a noble metal and an oxyphilic transition metal for promoting C–O bond cleavage is expected to find more applications in other biomass-related upgrading reactions.

Author contributions

Chen Cao and Weixiang Guan performed most of the catalyst preparation, characterizations and reaction tests and also wrote the draft. Qiaoyun Liu performed part of the catalyst preparations and stability testing. Lin Li helped to conduct CO-DRIFTS. Yang Su helped to perform HAADF-STEM imaging. Fei Liu, Aiqin Wang, and Tao Zhang conceived the idea and revised the paper.

Conflicts of interest

There are no conflicts to declare.

Acknowledgements

The authors are grateful for supports from the National Key R&D Program of China (2023YFA1506803), the National Natural Science Foundation of China (22209171, 22132006 and 22108259), and the NSFC Center for Single-Atom Catalysis (Grant No. 22388102).

References

1 T. Mizugaki, T. Yamakawa, Y. Nagatsu, Z. Maeno, T. Mitsudome, K. Jitsukawa and K. Kaneda, *ACS Sustainable Chem. Eng.*, 2014, **2**, 2243–2247.
2 T. Tong, X. Liu, Y. Guo, M. N. Banis, Y. Hu and Y. Wang, *J. Catal.*, 2018, **365**, 420–428.
3 F. Liu, Q. Liu, J. Xu, L. Li, Y.-T. Cui, R. Lang, L. Li, Y. Su, S. Miao, H. Sun, B. Qiao, A. Wang, F. Jérôme and T. Zhang, *Green Chem.*, 2018, **20**, 1770–1776.
4 Q. Liu, B. Qiao, F. Liu, L. Zhang, Y. Su, A. Wang and T. Zhang, *Green Chem.*, 2020, **22**, 3532–3538.
5 S. Liu, Y. Amada, M. Tamura, Y. Nakagawa and K. Tomishige, *Green Chem.*, 2014, **16**, 617–626.
6 B. Zhang, Y. Zhu, G. Ding, H. Zheng and Y. Li, *Green Chem.*, 2012, **14**, 3402–3409.
7 D. S. Pisal and G. D. Yadav, *ACS Omega*, 2019, **4**, 1201–1214.
8 A. Yamaguchi, Y. Murakami, T. Imura and K. Wakita, *ChemistryOpen*, 2021, **10**, 731–736.
9 T. Tong, Q. Xia, X. Liu and Y. Wang, *Catal. Commun.*, 2017, **101**, 129–133.
10 Y. Zhu, W. Zhao, J. Zhang, Z. An, X. Ma, Z. Zhang, Y. Jiang, L. Zheng, X. Shu, H. Song, X. Xiang and J. He, *ACS Catal.*, 2020, **10**, 8032–8041.
11 B. Qiao, A. Wang, X. Yang, L. F. Allard, Z. Jiang, Y. Cui, J. Liu, J. Li and T. Zhang, *Nat. Chem.*, 2011, **3**, 634–641.
12 A. Wang, J. Li and T. Zhang, *Nat. Rev. Chem.*, 2018, **2**, 65–81.
13 Y. Ren, Y. Tang, L. Zhang, X. Liu, L. Li, S. Miao, D. Su, A. Wang, J. Li and T. Zhang, *Nat. Commun.*, 2019, **10**, 4500–4508.
14 K. Tomishige, Y. Nakagawa and M. Tamura, *Green Chem.*, 2017, **19**, 2876–2924.
15 K. Chen, K. Mori, H. Watanabe, Y. Nakagawa and K. Tomishige, *J. Catal.*, 2012, **294**, 171–183.
16 S. Koso, N. Ueda, Y. Shinmi, K. Okumura, T. Kizuka and K. Tomishige, *J. Catal.*, 2009, **267**, 89–92.
17 S. Koso, I. Furikado, A. Shimao, T. Miyazawa, K. Kunimori and K. Tomishige, *Chem. Commun.*, 2009, **15**, 2035–2037.
18 B. Wang, F. Liu, W. Guan, A. Wang and T. Zhang, *ACS Sustainable Chem. Eng.*, 2021, **9**, 5705–5715.
19 M. Yang, X. Zhao, Y. Ren, J. Wang, N. Lei, A. Wang and T. Zhang, *Chin. J. Catal.*, 2018, **39**, 1027–1037.
20 Y. Zhang, L. Li, F. Liu, H. Qi, L. Zhang, W. Guan, Y. Liu, A. Wang and T. Zhang, *ACS Catal.*, 2022, **12**, 6302–6312.
21 Y. Zhang, F. Zhang, L. Li, H. Qi, Z. Yu, X. Liu, C. Cao, F. Liu, A. Wang and T. Zhang, *J. Catal.*, 2023, **417**, 301–313.

22 S. Liu, Y. Amada, M. Tamura, Y. Nakagawa and K. Tomishige, *Green Chem.*, 2014, **16**, 617–626.

23 Y. Nakagawa and K. Tomishige, *Catal. Today*, 2012, **195**, 136–143.

24 P. P. Upare, Y. Kim, K.-R. Oh, S. J. Han, S. K. Kim, D.-Y. Hong, M. Lee, P. Manjunathan, D. W. Hwang and Y. K. Hwang, *ACS Sustainable Chem. Eng.*, 2021, **9**, 17242–17253.

25 A. A. Shesterkina, O. P. Tkachenko, E. V. Shuvalova, G. I. Kapustin, V. B. Kazansky and L. M. Kustov, *Mendeleev Commun.*, 2019, **29**, 666–668.

26 W. Karim, C. Spreafico, A. Kleibert, J. Gobrecht, J. VandeVondele, Y. Ekinci and J. A. van Bokhoven, *Nature*, 2017, **541**, 68–71.

27 M. Tan, Y. Yang, Y. Yang, J. Chen, Z. Zhang, G. Fu, J. Lin, S. Wan, S. Wang and Y. Wang, *Nat. Commun.*, 2022, **13**, 1457–1464.

28 P. Reyes and H. Rojas, *React. Kinet. Catal. Lett.*, 2006, **88**, 363–369.

29 N. Lei, X. Zhao, B. Hou, M. Yang, M. Zhou, F. Liu, A. Wang and T. Zhang, *ChemCatChem*, 2019, **11**, 3903–3912.

30 S. Kobayashi, S. Kaneko, M.-a. Ohshima, H. Kurokawa and H. Miura, *Appl. Catal., A*, 2012, **417–418**, 306–312.

31 O. S. Alexeev, G. W. Graham, D.-W. Kim, M. Shelef and B. C. Gates, *Phys. Chem. Chem. Phys.*, 1999, **1**, 5725–5733.

32 M. J. Kappers and J. H. Vandermaas, *Catal. Lett.*, 1991, **10**, 365–373.

33 A. Siani, O. S. Alexeev, G. Lafaye and M. D. Amiridis, *J. Catal.*, 2009, **266**, 26–38.

34 X. Jin, R. Tsukimura, T. Aihara, H. Miura, T. Shishido and K. Nozaki, *Nat. Catal.*, 2021, **4**, 312–321.

35 J. P. Stassi, P. D. Zgolicz, S. R. de Miguel and O. A. Scelza, *J. Catal.*, 2013, **306**, 11–29.

36 Y. Wang, R. Qin, Y. Wang, J. Ren, W. Zhou, L. Li, J. Ming, W. Zhang, G. Fu and N. Zheng, *Angew. Chem., Int. Ed.*, 2020, **59**, 12736–12740.

37 N. S. Date, R. C. Chikate, H.-S. Roh and C. V. Rode, *Catal. Today*, 2018, **309**, 195–201.

38 H. Wei, X. Liu, A. Wang, L. Zhang, B. Qiao, X. Yang, Y. Huang, S. Miao, J. Liu and T. Zhang, *Nat. Commun.*, 2014, **5**, 5634–5641.

39 J. Wei, S.-N. Qin, J.-L. Liu, X.-Y. Ruan, Z. Guan, H. Yan, D.-Y. Wei, H. Zhang, J. Cheng, H. Xu, Z.-Q. Tian and J.-F. Li, *Angew. Chem., Int. Ed.*, 2020, **59**, 10343–10347.

40 J. Cao, S. Larasati, M. Yabushita, Y. Nakagawa, J. Wärnå, D. Y. Murzin, D. Asada, A. Nakayama and K. Tomishige, *ACS Catal.*, 2024, **14**, 1663–1677.

41 X. Li, X. I. Pereira-Hernández, Y. Chen, J. Xu, J. Zhao, C.-W. Pao, C.-Y. Fang, J. Zeng, Y. Wang, B. C. Gates and J. Liu, *Nature*, 2022, **611**, 284–288.

42 X. Liu, A. Wang, X. Yang, T. Zhang, C.-Y. Mou, D.-S. Su and J. Li, *Chem. Mater.*, 2009, **21**, 410–418.